

# Photoneutron Dataset Generation and Analysis at SLEGS\*

Zirui Hao,<sup>1,†</sup> Longxiang Liu,<sup>1</sup> Yue Zhang,<sup>1</sup> Hongwei Wang,<sup>1,2,3,‡</sup> Gongtao Fan,<sup>1,2,3,§</sup> Hanghua Xu,<sup>1</sup> Sheng Jin,<sup>2,3</sup> Yuxuan Yang,<sup>2</sup> Zhicai Li,<sup>1</sup> Pu Jiao,<sup>1</sup> Kaijie Chen,<sup>2</sup> Qiankun Sun,<sup>2,3</sup> Zhenwei Wang,<sup>2,3</sup> Mengdie Zhou,<sup>1,4</sup> Shan Ye,<sup>2,3</sup> Mengke Xu,<sup>2,3</sup> Xiangfei Wang,<sup>2,3</sup> and Yulong Shen<sup>1</sup>

<sup>1</sup>Shanghai Advanced Research Institute, Chinese Academy of Sciences, Shanghai 201210, China

<sup>2</sup>Shanghai Institute of Applied Physics, Chinese Academy of Sciences, Shanghai 201800, China

<sup>3</sup>University of Chinese Academy of Sciences, Beijing, 100080, Beijing, China

<sup>4</sup>School of Physics, Henan Normal University, Xinxiang 453007, China

Photoneutron data are increasingly used in basic research of nuclear physics and in applications of nuclear technology. China has long encountered a bottleneck in the independent measurement of photoneutron cross sections due to the lack of dedicated gamma sources. The Shanghai Laser Electron Gamma Source (SLEGS), based on laser Compton scattering (LCS), provides energy-tunable and quasi-monoenergetic gamma beams, opening up a new avenue for high-precision photonuclear research. This paper focuses on the Flat-Efficiency Detector (FED) array of SLEGS and its application in photoneutron cross section measurements. The systematic uncertainty of FED was verified to be 3.02% through the calibration of a <sup>252</sup>Cf neutron source. Additionally, it employs <sup>197</sup>Au and <sup>159</sup>Tb as case studies to demonstrate the format and processing methods of raw photoneutron data. The results confirm the application potential of SLEGS in the measurement of photoneutron cross sections, with SLEGS capable of supporting the independent acquisition of photoneutron data in China.

Keywords: Data descriptor, Raw data, Data repositories, Data sharing, Data reuse

## I. INTRODUCTION

Photonuclear reaction data are crucial across numerous fields, serving as a cornerstone for advancing nuclear science and facilitating a diverse array of practical applications. These applications encompass nuclear analysis, detection, diagnosis, gamma activation analysis, nuclear safeguard and verification technologies, nuclear waste transmutation, human radiotherapy absorbed dose calculations, and medical isotope production [1, 2]. For example, the accurate measurement of photonuclear data is indispensable for ensuring the safety, efficiency, and reliability of nuclear reactors, which are integral to China's sustainable development strategy. Within nuclear reactors, high-energy gamma rays can initiate photonuclear reactions with reactor materials, generating a significant number of photoneutrons that may influence neutron equilibrium and migration. Consequently, precise photonuclear data are critical for both reactor operations and essential safety assessments.

However, obtaining precise photonuclear data presents significant challenges. Currently, most available data are derived from sources of bremsstrahlung or in-flight positron annihilation gamma sources (e.g., those at Saclay and LLNL laboratories) [3], as well as theoretical calculations (including TENDL [4], ENDF [5], JENDL [6], and CENDL [7]). Accelerator-based gamma sources are limited to producing quasi-monochromatic gamma rays rather than truly

monochromatic ones. As a result, monochromatic cross sections must be inferred from quasi-monochromatic cross sections. Unfortunately, the extraction algorithms used for this purpose do not provide unique solutions, leading to discrepancies among global datasets. In China, the scarcity of gamma sources has further impeded the acquisition of independent experimental data for photonuclear reaction cross sections, thereby restricting the evaluation and practical utilization of photonuclear data.

SLEGS [8, 9] serves as a new gamma-ray source that delivers MeV energy  $\gamma$ -ray beams for photonuclear science and technology research [10, 11]. It is one of the 16 beamlines in the Shanghai Synchrotron Radiation Facility (SSRF) phase II [16]. Figure 1 shows the schematic view of the SLEGS beamline. The SLEGS (<https://CSTR.cn/31124.02.SSRF.BL03SSID>)  $\gamma$ -ray is generated through the interaction between the electron beam from SSRF (<https://CSTR.cn/31124.02.SSRF>) storage ring [13, 14] and the photons from a continuous wave (CW) COHERENT DIAMOND Cx-10 (10.64  $\mu$ m) CO<sub>2</sub> laser [15] in the SLEGS laser hutch. This laser operates flexibly, with a power range of 0.1 to 137 W, a frequency band of 1 to 100 kHz, and adjustable pulse width from 1 to 1000  $\mu$ s.

SLEGS generates quasi-monochromatic energy-tunable  $\gamma$ -ray beams in the energy range of 0.25–21.7 MeV by tuning the interaction angle of laser and electron beam (the corresponding inverse Compton scattering maximum energy is 0.66–21.1 MeV from 20 to 160 degrees, 21.7 MeV corresponds to 180 degrees), with a flux of  $2.1 \times 10^4$ – $1.2 \times 10^7$  photons/s and an energy spread of 5–15% in different collimator apertures. The greatest advantage of SLEGS lies in its ability to share beam-time with other beamline users and operate synchronously, which stands in sharp contrast to the exclusive operation mode typically adopted by existing international beamline facilities.

The adjustability of the interaction angle can be achieved

\* This work was supported by National Key Research and Development Program of China(No.2022YFA1602404, No.2023YFA1606901), the National Natural Science Foundation of China( No.12275338, No.12388102, No.U2441221), and the Key Laboratory of Nuclear Data Foundation (JCKY2022201C152)

† Corresponding author. Zirui Hao, haozr@sari.ac.cn

‡ Corresponding author. Hongwei Wang, wanghw@sari.ac.cn

§ Corresponding author. Gongtao Fan, fangt@sari.ac.cn

in approximately 10 minutes, significantly optimizing beam time utilization. The  $\gamma$ -rays are aligned by a  $\Phi$  (1-30) mm coarse collimator (C), a  $\Phi$  (1-30) mm fine collimator (F) and a three-hole collimator (T) with apertures of 1 mm, 2 mm, 3 mm. SLEGS was officially completed in December 2021 and has been open to users since January 2023.

## II. EXPERIMENTAL DESIGN AND DATA GENERATION

Photonuclear data primarily comprise photoneutron data, which represent the dominant excitation mode of the Giant Dipole Resonance (GDR) arising from the collective motion of atomic nuclei and constitute the largest component of the excitation function curve. Photoneutron data are currently measured using FED [17] at SLEGS. In the experiment, the photon-induced neutrons are then moderated by polyethylene before being captured by proportional  $^3\text{He}$  counters. Simultaneously, the residual  $\gamma$ -rays are attenuated by the external copper blocks and subsequently measured by a large  $\text{LaBr}_3$  detector ( $\Phi 76.2 \text{ mm} \times 101.6 \text{ mm}$ ) [18] or a BGO detector ( $\Phi 76.2 \text{ mm} \times 200 \text{ mm}$ ) [19].

The FED is a detector array specifically designed for photoneutron measurements, as illustrated in Fig. 2. It consists of 26 sets of  $^3\text{He}$  proportional counters embedded within a high-density polyethylene moderator measuring 500 mm in length, 450 mm in width, and 450 mm in height. To shield against environmental thermal neutrons, the polyethylene is fully encased on all six sides by 2 mm thick cadmium layers. Additionally, the entire assembly is surrounded by a 50 mm outer layer of polyethylene. At the center of the moderator lies a beam channel with a diameter of 26 mm, where the experimental target is precisely positioned. The collimated  $\gamma$ -rays irradiate the reaction target, typically with dimensions of  $\Phi(6-10) \text{ mm} \times (0.1-100) \text{ mm}$ , which is precisely aligned at the geometric center of the FED. Geant4 simulation studies have indicated that minor deviations in the target position have negligible effects on neutron measurements. The  $^3\text{He}$  proportional counters are arranged in three concentric rings at varying radial distances from the center: 65 mm (R1), 110 mm (R2), and 175 mm (R3). The inner ring (R1) comprises 6 counters, each with a 1-inch diameter and an effective length of 500 mm. The middle ring (R2) contains 8 counters, and the outer ring (R3) is equipped with 12 counters, each with a 2-inch diameter and the same 500 mm effective length. All 26 counters are filled with  $^3\text{He}$  gas at a pressure of 2 atm.

The high voltage applied to the  $^3\text{He}$  proportional counters is approximately 1 kV, with specific values of 950 V for the R1 and 1050 V for R2 and R3. This voltage is supplied by the CAEN A1589 module [20] housed within the high voltage power crate SY4527LC [21]. The system employs a total of three preamplifier modules, each integrating 16 channels. To address the long decay time characteristic of  $^3\text{He}$  proportional counters, the design incorporates waveform truncation, ensuring that the output signal decays rapidly after reaching its peak. This feature is implemented to minimize the system's dead time and enhance measurement efficiency.

Digital conversion is performed using Mesytec's MDPP-

16 [22] and MVME [23] Data Acquisition System (DAQ). The MDPP-16 is a regular data acquisition, internally solidified with firmware programs, Standard Charge Integrating Preamplifier (SCP), Peak sensing ADC (PADC), and other programs, which can directly convert the collected waveform data into digital output such as amplitude or area. In MDPP-16, the output pulses from the charge-sensitive preamplifier are first subjected to gain modification and low-noise amplification before converted to a 80 MHz ADC, and the analog signal is converted to a digital signal and sent to the FPGA firmware for signal reconstruction. The reconstructed signal uses the built-in trapezoidal filtering and fast-time filtering algorithm to obtain energy and time information. The MVME data acquisition system captures data in a compressed binary format, necessitating decompression and conversion to the CERN ROOT format [24] format using specialized code before analysis. The MVME data is archived in '\*.zip' files, which contain the raw data in '\*.mvclst' format, an MVME Analysis file named 'analysis.analysis', a log file 'messages.log', and a notes file 'mvme\_run\_notes.txt'. The binary raw data '\*.mvclst' can be directly decoded by MVME. However, MVME is not suitable for detailed analysis. Consequently, We have developed a decoding program to transform the binary file to the CERN ROOT format according to the MDPP-16 manual [22]. The resulting CERN ROOT file contains a single TTree named 'Tree;1', which includes branches for ADC (signal pulse height); Ch (channel number of MDPP-16), Flag (indicator for pile-up, overflow, or underflow events); Mod (MDPP-16 identifier, with two MDPP-16 modules in total); TDC (signal timestamp); CFD (TDC time difference); dt (time intervals between adjacent events), and EvN (debugging variable; a value of 0 signifies normal conditions). The ADC is utilized for neutron Q-spectra analysis. Ch and Mod are employed to determine the origin of the signal. TDC is used for period analysis and coincidence analysis in the DNM sorting for ( $\gamma$ , xn) ( $x=2, 3, \dots$ ) measurements.

All measurements were conducted using MVME, a ready-to-run, platform-independent, and open-source DAQ software package that integrates hardware configuration, run control, and online monitoring functionalities. The MVME interface and its operational block diagram are illustrated in Fig. 3. The system features pre-configured hardware settings programmed into the corresponding VME registers, significantly reducing the learning curve for new users. To optimize data acquisition rates, the MVME software utilizes the list sequencer mode of the MVLC controller. The online data monitoring and visualization system incorporates a three-tier analysis capability, enabling calibration, basic computations (such as sums and ratios), and 1D/2D histogram generation. Additionally, the software includes a built-in scripting language that facilitates the development of plug-in processes for complex data manipulation tasks. The system supports data storage rates of up to 50 MBytes per second. Specifically, for the MDPP-16 module, this translates to the capability of registering a 1 MHz event rate with simultaneous responses from 5 channels, while accurately measuring both amplitude and timing parameters.

The FED data acquisition system is composed of four pri-



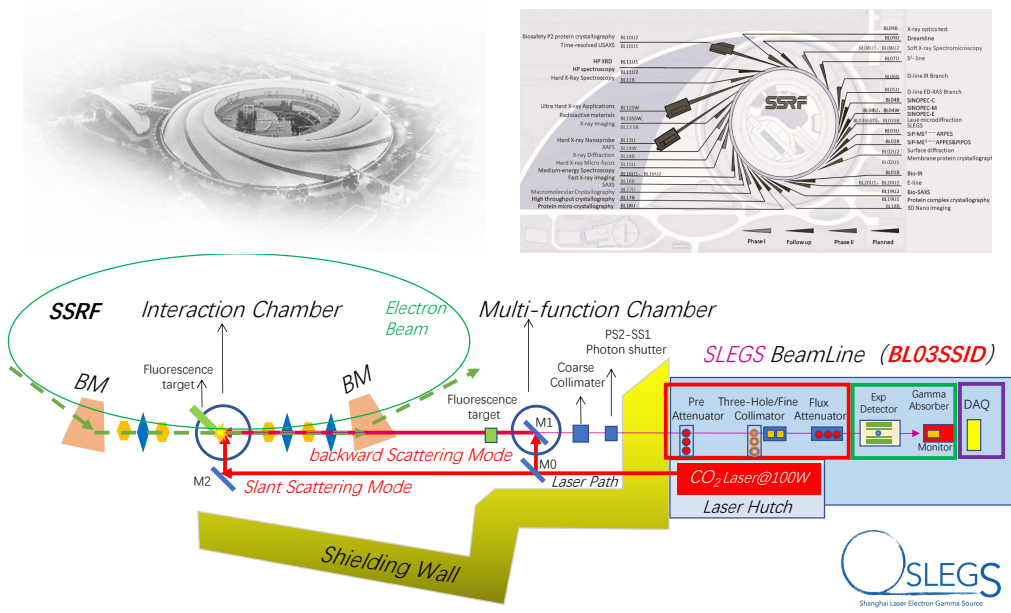


Fig. 1. (Color online) The schematic view of SLEGS beamline in SSRF.

many components. The first component is the data acquisition control interface, which is responsible for initiating or terminating data acquisition, configuring the MVLC connection mode with the data acquisition electronics, determining whether to record data, setting the duration of data acquisition, naming the data recording file, and choosing whether to segment the recording file by time period or file size. The second component is the VME electronic parameter configuration interface, which primarily handles the setup of the two MDPP-16 waveform digital samplers. This includes configuring their addresses to match the hardware settings, ensuring the firmware mode aligns with the hardware settings, and setting parameters such as integral and derivative time, shaping amplification time, rise time, and attenuation time for signal time filtering. The third component is the data analysis interface, which allows users to select the data source for analysis, perform necessary logical operations, and generate visual one-dimensional or two-dimensional histograms. The fourth component is the log interface, which outputs information related to the data acquisition process, such as the start and stop times of acquisition, configured electronic parameters, and any errors encountered. For example, if an error occurs during acquisition, it will be highlighted in red text on the interface, enabling users to quickly identify and diagnose the issue based on the provided information.

The BGO or LaBr<sub>3</sub> detector, used for  $\gamma$ -ray measurement, is powered by the A1589 module. Signals from the BGO or LaBr<sub>3</sub> detectors are digitized by the DT5730B module, with data acquisition managed by the CoMPASS system, typically operating in Pulse Height Analysis (PHA) mode. The acquired data is directly saved in **CERN ROOT** format. In a standard **CERN ROOT** file, a single Tree named Data\_R is

created. For preliminary data processing, three key Branches are commonly utilized: the "Channel" Branch identifies the specific DT5730B channel from which the signal was acquired; the "Timestamp" Branch records the arrival time of each event in picoseconds; and the "Energy" Branch represents the pulse amplitude of the detected signal.

### III. UNCERTAINTY ANALYSIS OF FED ARRAY

In the measurement of photoneutron cross sections, the primary sources of uncertainty arise from three key factors: the accuracy of the incident gamma energy spectrum, the uncertainty in neutron counts, and the thickness and density of the target. The uncertainty in neutron counts encompasses statistical fluctuations, uncertainty introduced by the neutron count extraction algorithm, and systematic uncertainties in the FED efficiency. The FED systematic uncertainty is influenced by several factors, including high voltage settings, target positioning, acquisition system configurations, and inherent detector fluctuations.

To quantify the FED systematic uncertainty, a detailed study was performed using a  $^{252}\text{Cf}$  neutron source with a known emission rate of  $361.3 \pm 10.8$  counts/s. The FED was carefully aligned within the experimental hutch to replicate the environmental background conditions of the actual experiment. Figure 4(a) illustrates a typical pulse height spectrum recorded by one of the  $^3\text{He}$  counters in the FED. Figure 4(b) presents the simulated neutron energy distribution derived from the  $^{252}\text{Cf}$  standard neutron source, providing a reference for understanding the detector's response and systematic effects.

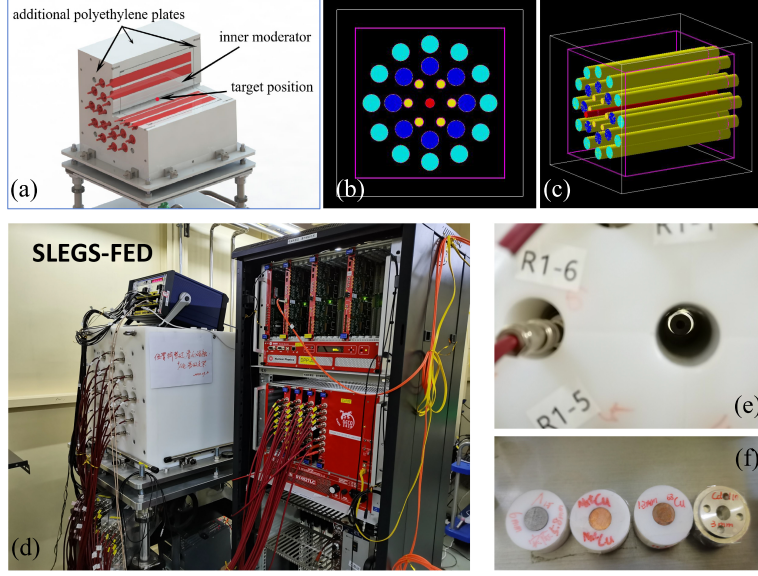


Fig. 2. (Color online) (a) The schematic diagram of the FED. (b) and (c) are the construction used in Geant4 simulations, showing the front and side views, respectively. (d) The photograph of the FED and its electronics, including the pre-amplifier, high-voltage power supply, and data acquisition (DAQ). (e) The photograph of the central channel of the FED, with a target placed inside. (f) The photograph of the experimental target.

The  $^3\text{He}$  counters are operated in the proportional region, where the detector efficiency exhibits minimal dependence on the applied high voltage. To determine the optimal operating conditions, the efficiency of each detector ring has been tested at a range of high voltages, with each voltage setting evaluated for 1 hour. Based on these tests, the optimal operating voltages were established as 950 V for Ring-1, 1050 V for Ring-2 and Ring-3. The total detector efficiencies were measured to be  $41.92 \pm 1.25\%$ ,  $42.10 \pm 1.25\%$ , and  $41.91 \pm 1.25\%$  (statistical uncertainty only) at high voltage deviations of -50 V, 0 V, and +50 V, respectively. These results indicate that the detector efficiency remains relatively stable even with a 50 V variation in high voltage, as shown in Fig. 4(c). Assuming a linear relationship between detector efficiency and high voltage, the systematic uncertainty introduced by high voltage fluctuations is estimated to be 0.02%, given that the CAEN A1589 module maintains a voltage deviation of less than 1 V.

The uncertainty associated with the target position was studied by systematically moving the  $^{252}\text{Cf}$  source along the central tunnel of the FED moderator. The relationship between detector efficiency and the source position is illustrated in Fig. 4(d). The efficiency distribution exhibits asymmetry, which can be attributed to the asymmetrical construction of the detector. Nevertheless, the efficiency remains relatively stable when the source is displaced slightly around the central position. The systematic uncertainty contribution from the source position is estimated to be 0.10% for a deviation of 1 cm.

TABLE 1. The systematic uncertainty of the FED array.

Uncertainty Factors	Value
High voltage	0.02%
Preset DAQ parameters	0.17%
Target position bias	0.10%
Efficiency fluctuation	0.26%
$^{252}\text{Cf}$ activity uncertainty	3.00%
Total uncertainty	3.02%

In addition to the uncertainties previously discussed, deviations may also originate from the parameters configured in the data acquisition system. The fine-tuning of key parameters and their corresponding detector efficiencies are detailed in Table 1. A set of reliable parameters, proven to be effective in signal amplification and exhibiting minimal correlation with detector efficiency, has been established. Following a long-term continuous measurement, the stability of the entire detector system has been confirmed, with an efficiency fluctuation measured at 0.26%.

Table 1 provides a summary of the upper limits of uncertainties for the detector system. The uncertainty arising from the maximum high voltage deviation (1 V) is 0.02%. The efficiency uncertainty due to source position bias is 0.10%, assuming a maximum deviation of 1 cm from the geometric center. By quadratically summing the uncertainties listed in Table 1 with the  $^{252}\text{Cf}$  activity uncertainty of 3.0%, the total systematic uncertainty of the FED is determined to be 3.02%.

Figure 5(a) displays the Geant4-simulated efficiency curve.

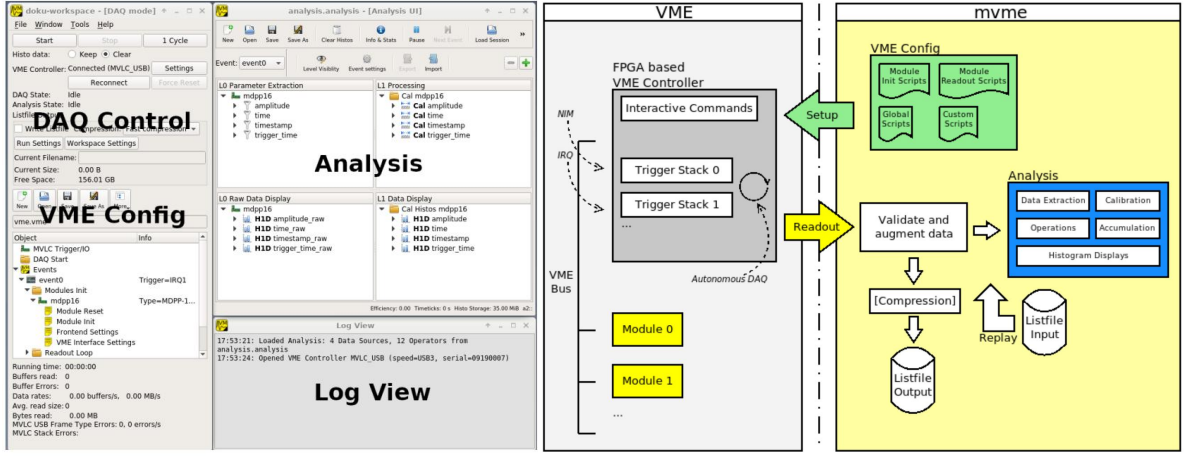


Fig. 3. (Color online) The MVME Software GUI Window and Block Diagram.

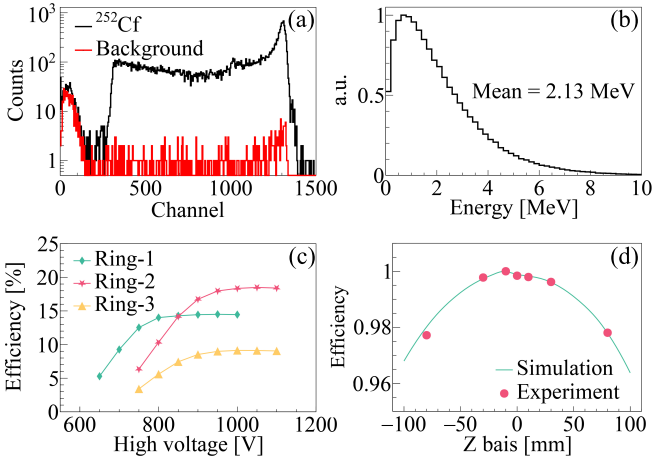


Fig. 4. (a) A typical spectrum measured with the  $^{252}\text{Cf}$  neutron source (black line) compared to the environmental background (red line). (b) The simulated neutron energy distribution from the  $^{252}\text{Cf}$  source. (c) The detector efficiency for the three rings as a function of high voltage. (d) Detector efficiency as a function of the source position along the central tunnel of the FED.

The total detector efficiency rises from 35.64% at 50 keV to 42.32% at 1.65 MeV and gradually decreases to 40.69% at 3 MeV for neutrons following a Maxwell-Boltzmann energy distribution. The efficiency calibrated using the  $^{252}\text{Cf}$  source, measured at  $42.10 \pm 1.25\%$ , is indicated on the curve at 2.13 MeV, corresponding to the average energy of the  $^{252}\text{Cf}$  neutron spectrum. In the experiment [25, 26], the average neutron energy is determined using the Ring-Ratio (RR) technique

[27, 28], which is defined as the ratio of counts in the outer ring to those in the inner ring, as illustrated in Fig. 5(b). While the RR technique provides only an approximate average energy, which may deviate from the actual value, the flat efficiency profile of the detector ensures that the difference between the calculated and actual detector efficiency remains negligible.

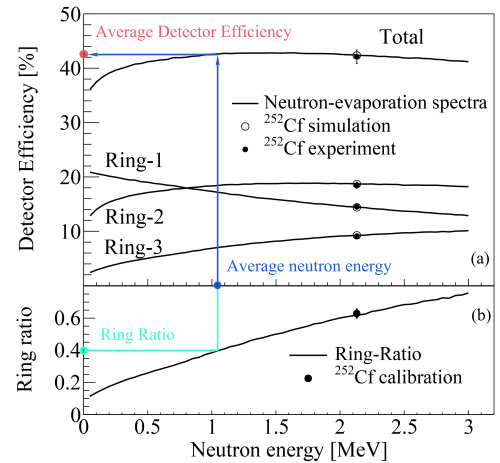


Fig. 5. (Color online) The detector efficiency and RR curve. The RR technique is shown in color lines.



#### IV. PHOTONEUTRON CROSS SECTION DATA ANALYSIS

The photoneutron cross section is defined as

$$\int_{S_n}^{E_{max}} n_\gamma(E_\gamma) \sigma_{\gamma n}(E_\gamma) dE_\gamma = \frac{N_n}{N_t N_\gamma \xi \epsilon_n g}. \quad (1)$$

Here,  $n_\gamma(E_\gamma)$  represents the normalized energy distribution of the incident  $\gamma$ -rays. The term  $\sigma_{\gamma n}(E_\gamma)$  denotes the monochromatic cross section, which is the quantity to be determined.  $S_n$  is the neutron separation energy of the target nucleus.  $N_n$  corresponds to the number of detected photoneutrons, while  $N_\gamma$  is the number of  $\gamma$ -rays incident on the target. The average detector efficiency,  $\epsilon_n$ , is derived using the RR technique.  $N_t$  represents the number of target nuclei per unit area. The correction factor for target self-attenuation,  $\xi$ , is given by  $\xi = (1 - e^{-\mu t})/(\mu t)$ , where  $\mu$  is the attenuation coefficient for  $\gamma$ -rays, and  $t$  is the target thickness. Finally,  $g$  is the fraction of the  $\gamma$ -ray flux above the neutron separation energy  $S_n$ .

$$g = \frac{\int_{S_n}^{E_{max}} n_\gamma(E_\gamma) dE_\gamma}{\int_0^{E_{max}} n_\gamma(E_\gamma) dE_\gamma}. \quad (2)$$

##### A. Data preprocessing

The quantities  $N_n$  and the  $N_\gamma$  are measured parameters obtained from the FED and BGO (or LaBr<sub>3</sub>) detectors, respectively. In the data analysis program, the incident  $\gamma$ -ray spectra on the target are processed, which not only provides  $N_\gamma$  but also yields the normalized  $\gamma$ -ray energy spectra. These spectra are essential for determining the monochromatic cross sections. The extraction of  $N_n$  is achieved by analyzing the time distribution of the detector signals, leveraging the pulsed nature of the laser and the timestamp recorded by the DAQ system for each detected signal. This section outlines the methodology for extracting  $N_n$  and  $N_\gamma$ .

The SSRF operates in top-up mode, with a storage ring circumference of 432 meters, resulting in a 1.44  $\mu$ s revolution time for electrons. The electron beam is distributed across 720 buckets, of which approximately 500 are filled with electron bunches. These bunches are organized into 4 groups, with a 2 ns interval between adjacent bunches within each group. The CO<sub>2</sub> laser operates in pulsed mode, synchronized with a dedicated trigger for laser output. Typically, the laser operates at a power of 5 W, with a pulse period of 1000  $\mu$ s and a pulse width of 50  $\mu$ s. Fig. 6 provides a schematic diagram illustrating the time distribution of the laser pulses and electron bunches.

The laser period is nominally set to 1000  $\mu$ s, but in practice, it exhibits slight variations around this value. Fortunately, these variations do not impact the data analysis process. To accurately determine the time distribution of signals within a laser period, it is necessary to analyze the precise period for each data file. This is achieved by scanning a range of

possible laser periods and identifying the optimal period that results in the narrowest full width at half maximum (FWHM) of the time distribution spectrum, as illustrated in Fig. 7(a). Once the optimal period is determined, the background is subtracted according to the time distribution corresponding to this period.

The neutron count  $N_n$  is directly extracted from the neutron time distribution spectrum, as shown in Fig. 7(c). Similarly, the  $\gamma$ -ray time distribution spectrum (Fig. 7(b)) is used to isolate the LCS  $\gamma$ -ray spectrum from the electron bremsstrahlung background, resulting in the LCS detector response spectrum (represented by the orange line in Fig. 7(d)). The incident energy spectrum on the detector is then calculated using the direct unfolding method, as detailed in the article [29].

Figure 8 compares the incident gamma energy spectrum obtained from the direct unfolding method (red solid line), the detector response spectrum (blue dashed line), and the reconstructed spectrum (black solid line). Finally, the energy spectrum incident on the target is computed by accounting for the thickness and attenuation coefficient of the attenuator (Cu) and the target material. Integrating this gamma energy spectrum yields the total number of incident  $\gamma$ -rays,  $N_\gamma$ .

In the  $N_n$  extraction algorithm, each ring is analyzed as an independent unit, which is essential because the RR technique relies on the counts from Ring-3 and Ring-1. As illustrated by the colored arrows in Fig. 5, the process begins by calculating the ratio of Ring-3 to Ring-1 (cyan dot). Using the RR curve, the average neutron energy is determined (blue dot). Finally, the average neutron efficiency  $\epsilon_n$  is derived from the efficiency curve (red dot). The right side of Equation 1 represents the monochromatic approximation cross section (also referred to as the folded cross section), as the incident gamma rays are quasi-monochromatic in nature.

##### B. Monochromatic Photoneutron cross section

The monochromatic approximation cross section represents an averaged cross section weighted by the normalized incident gamma spectrum. In this section, the algorithm for extracting monochromatic cross sections is introduced. The monochromatic approximation cross section can be expressed as:

$$\sigma_f = \mathbf{D}\sigma. \quad (3)$$

The quantity  $\sigma_f$  represents a monochromatic approximation cross section array, where each element corresponds to the monochromatic approximation cross section measured at discrete beam energies ( $E_\gamma$ ). The array  $\sigma$  contains the monochromatic cross sections. The matrix  $\mathbf{D}$  is constructed from normalized incident gamma energy distributions spanning from  $S_n$  to  $E_{max}$ . Equation 4 is the expanded form of Eq. 3. The number of rows ( $N$ ) in  $\mathbf{D}$  corresponds to the number of discrete beam energies, while the number of columns ( $M$ ) corresponds to the number of bins in the incident gamma spectrum from  $S_n$  to  $E_{max}$ .

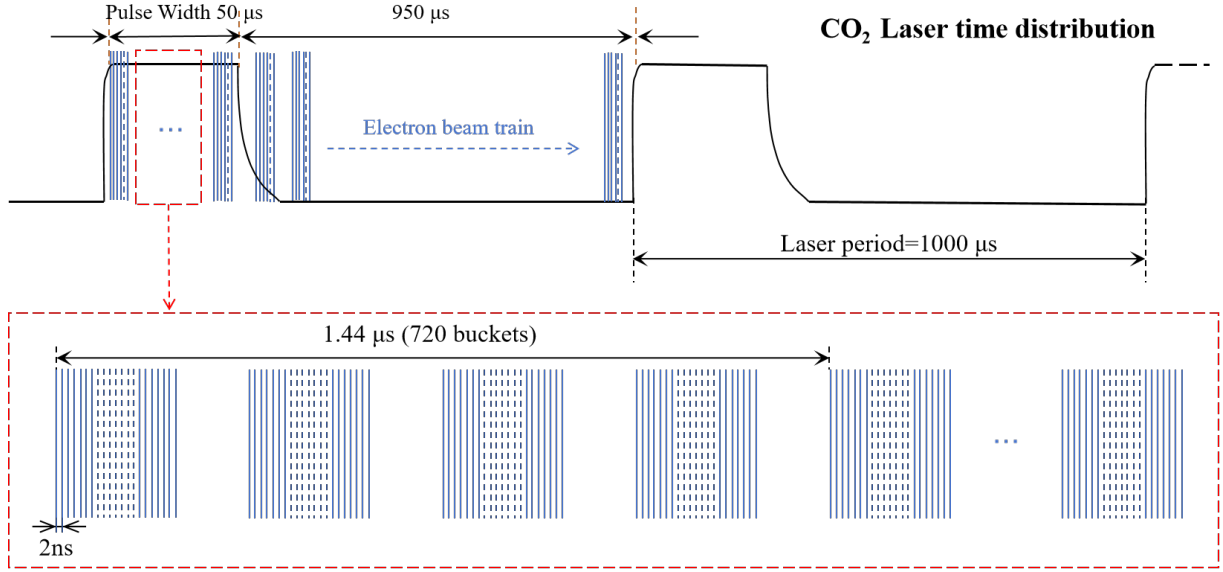


Fig. 6. The time distribution of the laser pulses and electron bunches at SLEGS.

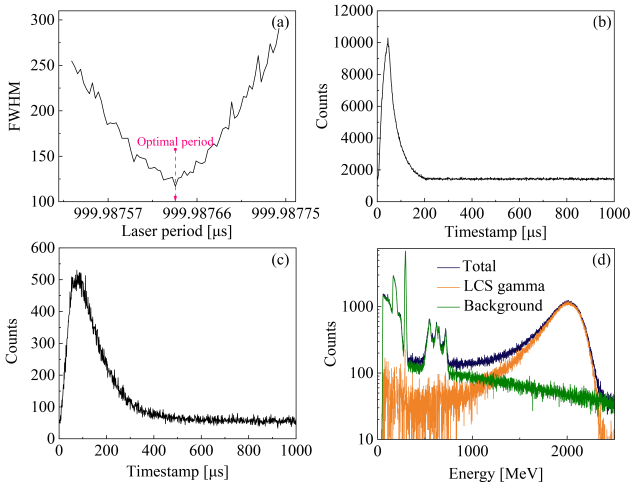


Fig. 7. (Color online) (a) A scan of the FWHM to determine the optimal laser period. (b) The  $\gamma$ -ray time distribution at the optimal laser period. (c) The neutron time distribution at the optimal laser period. (d) The LCS detector response spectrum (orange line), obtained by subtracting the bremsstrahlung background (green line) from the total detector response spectrum (black line).

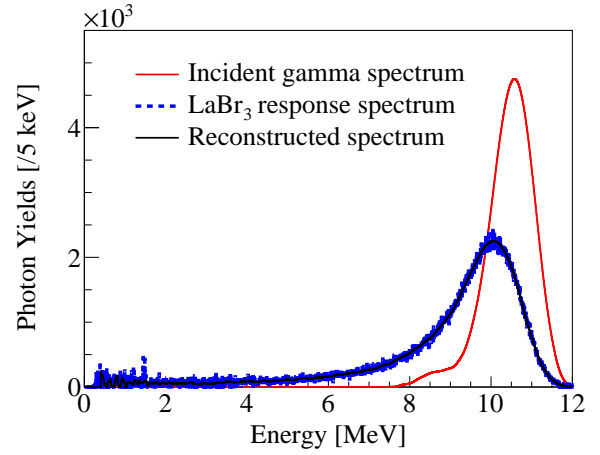


Fig. 8. (Color online) The incident gamma spectrum (red solid line) obtained using the direct unfolding method, alongside its corresponding response spectrum (blue dashed line). The reconstructed spectrum (black solid line) is derived by folding the incident gamma spectrum with the detector response matrix.

denoted as  $\sigma^0$  in the first iteration, and substitute it into Eq. 3 to obtain  $\sigma_f^0$ .

(2) Then, based on the difference between  $\sigma_{\text{exp}}$  and  $\sigma_f^0$ , adjust  $\sigma^0$  to obtain  $\sigma^1$ .

$$\sigma^1 = \sigma^0 + (\sigma_{\text{exp}} - \sigma_f^0). \quad (5)$$

It is worth noting that the dimension of  $\sigma^0$  ( $M$ ) is much larger than that of  $\sigma_{\text{exp}}$  and  $\sigma_f^0$  ( $N$ ). To perform Eq. 5, it is necessary to expand the dimensions of  $\sigma_{\text{exp}}$  and  $\sigma_f^0$  to  $M$ .

(3) The  $i$ -th iteration follows the same algorithm, given by

$$\begin{pmatrix} \sigma_1 \\ \sigma_2 \\ \vdots \\ \sigma_N \end{pmatrix}_f = \begin{pmatrix} D_{11} & D_{12} & \dots & D_{1M} \\ D_{21} & D_{22} & \dots & D_{2M} \\ \vdots & \vdots & \ddots & \vdots \\ D_{N1} & D_{N2} & \dots & D_{NM} \end{pmatrix} \begin{pmatrix} \sigma_1 \\ \sigma_2 \\ \vdots \\ \sigma_M \end{pmatrix}. \quad (4)$$

An unfolding iteration method is employed to extract the monochromatic cross section  $\sigma$ :

(1) First, assign a value to  $\sigma$ , for example,  $[1, 1, 1, \dots, 1]^T$ ,

$$\sigma_f^i = \mathbf{D}\sigma^i, \quad (6)$$

$$\sigma_f^{i+1} = \sigma^i + (\sigma_{\text{exp}} - \sigma_f^i). \quad (7)$$

The  $\chi^2$  between  $\sigma_{\text{exp}}$  and  $\sigma_f^{i+1}$  is recorded in each iteration. The iteration procedure stops when  $\chi^2$  converges.

## TECHNICAL VALIDATION

Figure 9 presents a comparison of monochromatic cross sections for  $^{197}\text{Au}$  and  $^{159}\text{Tb}$  of the SLEGS experiment with data obtained from other laboratories. The cross section data will be formally published somewhere else. The data shown in this manuscript is only to illustrate the rationality of the data processing method.

The entire process of photonuclear neutron cross section measurement and data analysis is illustrated and summarized in Fig. 10. Notably, the methodology for measuring the  $(\gamma, 2n)$  cross section is currently under development, as indicated by the gray-colored section. A series of photoneutron experiments at SLEGS has been successfully completed, and the measurement data are being analyzed. These results will be progressively published to facilitate user access and verification, particularly for their inclusion in photonuclear data compilation and evaluation within the Chinese Nuclear Data Library (CENDL/PD). [30]

## USAGE NOTES

**1. Reaction Channels:** Photoneutron reaction is one of several reaction channels in photonuclear processes. SLEGS is equipped to measure  $(\gamma, 1n)$  cross sections. However, the methodology for  $(\gamma, 2n)$  cross section measurements is still under development. Due to the energy limitations of SLEGS, reactions beyond  $(\gamma, 2n)$  are not feasible.

**2. Quasi-Monochromatic Cross Sections:** The quasi-monochromatic cross section is an averaged cross section weighted by the normalized incident gamma spectra. As a result, fine structures in certain cross sections may be smoothed out.

**3. Unfolding Program Capabilities:** The  $(\gamma, 1n)$  photoneutron cross section unfolding program not only extracts monochromatic cross sections at measured energy points but also provides numerical cross section values within the measured energy range. Additionally, it can predict cross sections slightly beyond the measured energy limits.

**4. Data Availability:** The raw data for  $^{197}\text{Au}(\gamma, 1n)$  and  $^{159}\text{Tb}(\gamma, 1n)$  have been uploaded to the Science Data Bank [31, 32]. The monochromatic cross section data are also accessible through [33]. The raw data set includes a description list detailing the data generated by MVME and DT5730B, along with the corresponding attenuation thicknesses. From this, neutron counts and gamma counts (gamma spectra) can be extracted. The monochromatic cross section data are available in Ref. [33].

**5. Experimental Spectrometers:** SLEGS employs two types of photoneutron measurement spectrometers: the FED and the Time-of-Flight (TOF) spectrometer, with the TOF methodology currently under active investigation. Additionally, SLEGS has developed other experimental setups, including a Nuclear Resonance Fluorescence (NRF) spectrometer and a Light Charged Particle (LCP) spectrometer. These instruments generate unique datasets, which will be thoroughly presented and analyzed in future studies.

## CODE AVAILABILITY

The photoneutron cross section data processing program primarily comprises the following components: conversion of MVME binary data to CERN ROOT format, extraction of photoneutron counts, isolation of LCS gamma spectra, unfolding of the incident gamma spectrum, calculation of quasi-monochromatic cross sections, and extraction of monochromatic cross sections. SLEGS will provide comprehensive experimental programs and detailed user guidelines to researchers applying for photoneutron cross section measurement experiments, ensuring a streamlined and efficient experimental process.

## ACKNOWLEDGMENTS

The authors express their heartfelt gratitude to the colleagues from the Shanghai Light Source' Accelerator Department and Beam Line Engineering Department for their exceptional technical support. Furthermore, they extend their appreciation to the collaborative companies and research units for their invaluable contributions and assistance, which were pivotal to the successful execution of this work.

## AUTHOR CONTRIBUTIONS STATEMENT

Hongwei Wang and Gongtao Fan spearheaded the construction of the SLEGS beamline and experimental station. Zirui Hao and Longxiang Liu conducted methodological research and measurements related to the FED. Hanghua Xu, Yue Zhang, Yuxuan Yang, Sheng Jin, Kaijie Chen, Zhicai Li, Pu Jiao, Qiankun Sun, Mengdie Zhou, Shan Ye, Zhenwei Wang, Mengke Xu, Xiangfei Wang, and Yulong Shen participated in the experimental work.

Zirui Hao, Gongtao Fan, and Hongwei Wang contributed to the writing, review, and editing of the manuscript. All authors engaged in discussions of the results and reviewed the manuscript.

## COMPETING INTERESTS

The authors declare that they have no conflict of interest.



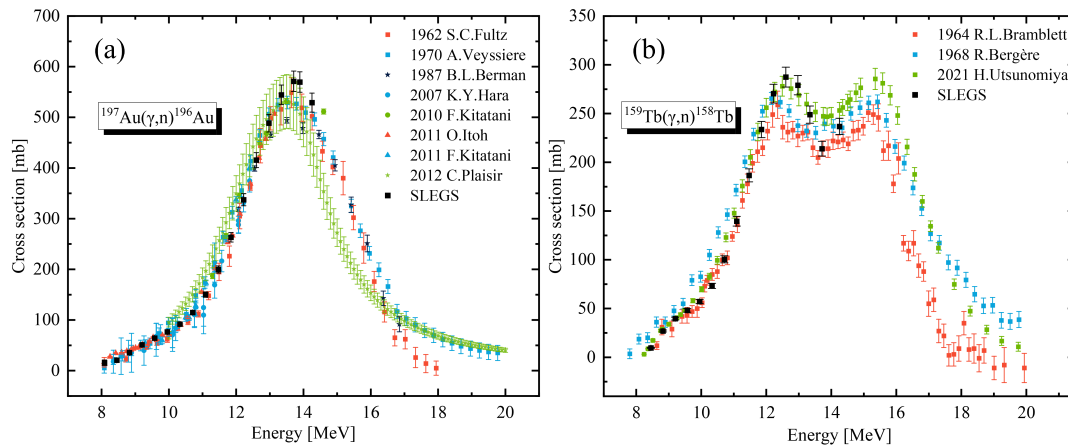


Fig. 9. (Color online) The measured photoneutron cross section of (a)  $^{197}\text{Au}$  and (b)  $^{159}\text{Tb}$  at SLEGS.

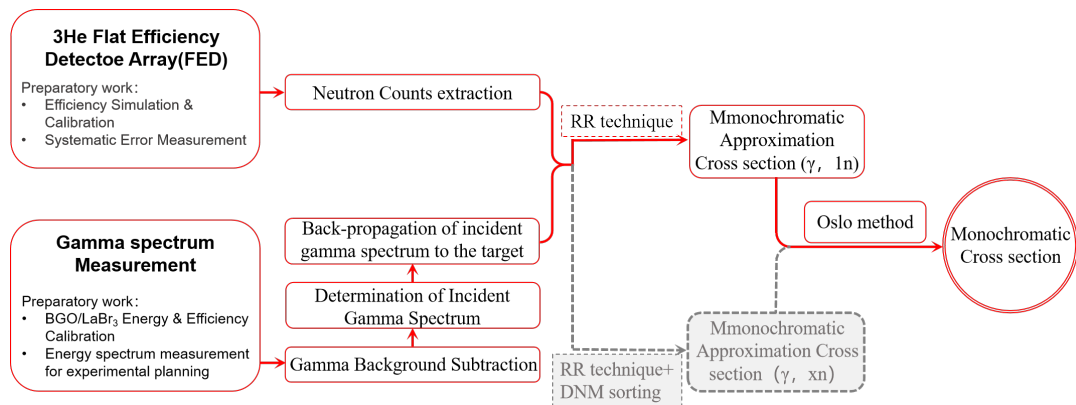


Fig. 10. (Color online) The photoneutron cross section measurement method at SLEGS is outlined, encompassing preliminary studies such as offline testing of the FED and  $\gamma$ -beam measurements, as depicted in the diagram. The methodology for measuring the  $(\gamma, 2n)$  cross section, currently under development, is highlighted in gray.

## FIGURES & TABLES

eters used for the SLEGS photoneutron cross section measurements are summarized in Table 3.

## REFERENCES

- A list of research articles related to SLEGS and the FED array is provided in Specification Table 2, while the key parameters used for the SLEGS photoneutron cross section measurements are summarized in Table 3.
- [1] A.G.Kazakov, T.Y.Ekatova, J.S.Babenya, Photonuclear production of medical radiometals: a review of experimental studies. *J. Radioanal. Nucl. Chem.* **328**, 493–505 (2021). doi:10.1007/s10967-021-07683-2
  - [2] X.Pang, B.H.Sun, L.H.Zhu, et al., Progress of photonuclear cross sections for medical radioisotope production at the SLEGS energy domain. *Nucl. Sci. Tech.* **34** (2023). doi:10.1007/s41365-023-01339-4
  - [3] S.S.Dietrich, B.L.Berman, Atlas of photoneutron cross sections obtained with monoenergetic photons. *Atom. Data Nucl. Data Tables* **38**, 199–338 (1988). doi:10.1016/0092-640X(88)90033-2
  - [4] A.J.Koning, D.Rochman, J.C.Sublet, et al., TENDL: Complete nuclear data library for innovative nuclear science and technology. *Nucl. Data Sheets* **155**, 1–55 (2019). doi:10.1016/j.nds.2019.01.002
  - [5] D.A.Brown, M.B.Chadwick, R.Capote, et al., ENDF/B-VIII.0: The 8th major release of the nuclear reaction data library with CIELO-project cross sections, new standards and thermal scattering data. *Nucl. Data Sheets* **148**, 1–142 (2018). doi:10.1016/j.nds.2018.02.001
  - [6] O.Iwamoto, N.Iwamoto, S.Kunieda, et al., Japanese evaluated nuclear data library version 5: JENDL-5. *J. Nucl. Sci. Technol.* **60**, 1–60 (2023). doi.org/10.1080/00223131.2022.2141903

TABLE 2. Specifications Table.

Subject	Nuclear physics
Specific subject area	Experimental data
Data format	Raw/Analyzed
Type of data	Table and Figure
How data were acquired	Measurements using a Flat-Efficiency Detector (FED) array
Parameters for data collection	Photoneutron cross section data.
Description of data collection	Data were collected by saving list-mode detector array during acquisitions.
Data collection	The data were collected from 2020 using the SLEGS gamma beam and FED array.
Data source location	Institution: Shanghai Advanced Research Institute,CAS
	Country: China
Data accessibility	Repository name: Science Data Bank
	Data identification number:
	<a href="https://cstr.cn/31253.11.sciencedb.19543">https://cstr.cn/31253.11.sciencedb.19543</a>
	<a href="https://cstr.cn/31253.11.sciencedb.19552">https://cstr.cn/31253.11.sciencedb.19552</a>
	<a href="https://cstr.cn/31253.11.sciencedb.19582">https://cstr.cn/31253.11.sciencedb.19582</a>
	Direct URL to data:
	<a href="https://doi.org/10.57760/sciencedb.19543">https://doi.org/10.57760/sciencedb.19543</a>
	<a href="https://doi.org/10.57760/sciencedb.19552">https://doi.org/10.57760/sciencedb.19552</a>
	<a href="https://doi.org/10.57760/sciencedb.19582">https://doi.org/10.57760/sciencedb.19582</a>
Related research article	Z.R.Hao, Nuclear Techniques (In Chinese), 43,9(2020). doi:10.11889/j.0253-3219.2020.hjs.43.110501. Z.R.Hao, et al., NIMA:1013 (2021) 165638. doi.org/10.1016/j.nima.2021.165638 H.H.Xu, et al., NIMA1033, 166742(2022). doi:10.1016/j.nima.2022.166742. H.W.Wang, et al., Nucl. Sci.Tech., 33, 87 (2022). doi:10.1007/s41365-022-01076-0. Z.R.Hao, et al., Nucl. Sci. Tech. 35(3), 65 (2024) doi: 10.1007/s41365-024-01425-1. Z.R.Hao, NIMA1068, 169748 (2024).doi:10.1016/j.nima.2024.169748. Z.R.Hao,et al., NIMA1013, 165638 (2021). doi:10.1016/j.nima.2021.165638. L.X.Liu,et al., Nucl.Sci.Tech.,35,111(2024). doi:10.1007/s41365-024-01469-3 L.X.Liu, et al., NIMA1063, 169314 (2024). doi:10.1016/j.nima.2024.169314. Z.C.Li et al., NIMB559(2025) 165595,https://doi.org/10.1016/j.nimb.2024.1655

TABLE 3. The main parameters of SLEGS and FED array for photoneutron cross section measurement.

Parameter Name/Units	Value or Mode
Electron Energy/GeV	3.5
Beam Current/mA	180-220
SSRF Operation Mode	Topup or Decay
CO <sub>2</sub> Laser Power/W	0.1-20,20-137(Adjustable)
Duty Cycle and Pulse Period /us	50/1000(Adjustable)
Coarse Collimator Diameter/mm	0-5,8,10,20,30(Adjustable)
Fine Collimator Diameter/mm	0-30(Adjustable)
Three-hole Collimator Diameter/mm	0,1,2,3,Empty(Fixed)
Copper Internal Attenuator/mm	0-640 (Adjustable)
Copper External Attenuator/mm	0-1000(Adjustable)
X-rays spot Monitor	MiniPIX [34]
$\gamma$ -rays spot Monitor	Gamma Spot Monitor- GSM
Gamma Beam Flux Monitor	LaBr <sub>3</sub> or BGO(Large size)
Monitor's DAQ	CAEN CoMPASS
Photoneutron Detector Array	FED Array
FED Array DAQ	Mesytec MVME

- [9] H.H.Xu,G.T.Fan,H.W.Wang,et al., Interaction chamber for laser Compton slant-scattering in SLEGS beamline at Shanghai Light Source. Nuclear Instruments and Methods in Physics Research Section A: Accelerators, Spectrometers, Detectors and Associated Equipment **1033**, 166742 (2022). doi:10.1016/j.nima.2022.166742
- [10] H.W.Wang,G.T.Fan,L.X.Liu et al., Development and Prospect of Shanghai Laser Compton Scattering Gamma Source. Nuclear Physics Review(In Chinese) **37** (2020). doi:10.11804/NuclPhysRev.37.2019043
- [11] H.W.Wang,G.T.Fan,L.X.Liu, et al., Commissioning of laser electron gamma beamline SLEGS at SSRF. Nucl. Sci. Tech. , 033 (2022). doi:10.1007/s41365-022-01076-0
- [12] K.J.Chen,L.X.Liu,Z.R.Hao, et al., Simulation and test of the SLEGS TOF spectrometer at SSRF. Nucl. Sci. Tech. **34** (2023). doi:10.1007/s41365-023-01194-3
- [13] L.X.Liu,H.W.Wang,G.T.Fan, et al., The SLEGS beamline of SSRF. Nucl. Sci. Tech. **35** (2024). doi:10.1007/s41365-024-01469-3
- [14] Z.R.Hao,H.H.Xu,G.T.Fan, et al., Gamma spot monitor at SLEGS beamline. Nucl. Instrum. Methods Phys. Res. Sect. A-Accel. Spectrom. Dect. Assoc. Equip. **1068** (2024). doi:10.1016/j.nima.2024.169748
- [15] DIAMOND C/Cx Series, low power CO<sub>2</sub> Lasers, <https://www.coherent.com/lasers/co2/diamond-c-cx-series>
- [16] R.Z.Tai, Z.T.Zhao, Overview of SSRF phase-II beamlines. Nucl. Sci. Tech. **35** (2024). doi:10.1007/s41365-024-01487-1
- [17] Z.R.Hao,G.T.Fan,L.X.Liu, et al., Design and simulation of 4 $\pi$  flat-efficiency <sup>3</sup>He neutron detector array. Nuclear Techniques (in Chinese) **43**, 110501–110501 (2020). doi:10.11889/j.0253-

- [7] Z.G.Ge,R.R.Xu,H.C.Wu,et al., CENDL-3.2:The new version of Chinese general purpose evaluated nuclear data library, EPJ Web of Conferences **239**,(2020). doi:10.1051/epjconf/202023909001
- [8] Z.R.Hao,G.T.Fan,H.W.Wang,et al., Collimator system of SLEGS beamline at Shanghai Light Source. Nuclear Instruments and Methods in Physics Research Section A: Accelerators, Spectrometers, Detectors and Associated Equipment **1013**, 165638 (2021). doi:10.1016/j.nima.2021.165638

- 3219.2020.hjs.43.110501
- [18] Lanthanum Bromide(LaBr<sub>3</sub>) detector from LUXIUM, <https://www.luxiumsolutions.com/radiation-detection-scintillators/crystal-scintillators/lanthanum-bromide-labr3>
- [19] Bismuth germanate(BGO) Detector from SICCAS, Shanghai SICCAS high technology corporation, <http://www.siccas.com/bgo.aspx?pld=42>
- [20] CAEN A1589, 8 Channel  $\pm 2.5$  kV/500  $\mu$ A 4 Quadrant Bipolar Board, <https://www.caen.it/products/a1589/>
- [21] CAEN SY4527LC, Universal Multichannel Power Supply System (Low Cost), <https://www.caen.it/products/sy4527lc/>
- [22] Mesytec MDPP-16, fast high resolution time and amplitude digitizer, <https://www.mesytec.com/products/nuclear-physics/MDPP-16.html>
- [23] Mesytec MVME - Mesytec VME Data Acquisition, <https://www.mesytec.com/downloads/mvme.html>
- [24] ROOT: analyzing petabytes of data, scientifically. <https://root.cern.ch/>
- [25] B.L.Berman,J.T.Caldwell,R.R.Harvey, et al., Photoneutron Cross Sections for <sup>90</sup>Zr, <sup>91</sup>Zr, <sup>92</sup>Zr, <sup>94</sup>Zr, and <sup>89</sup>Y. Physical Review **162**, 1098 (1967). doi:10.1103/PhysRev.162.1098
- [26] B.L.Berman,S.C.Fultz, Measurements of the giant dipole resonance with monoenergetic photons. Rev.Mod.Phys. **47**, 713–761 (1975). doi:10.1103/RevModPhys.47.713
- [27] O.Itoh, H.Utsunomiya, H.Akimune, et al., Photoneutron Cross Sections for Au Revisited: Measurements with Laser Compton Scattering  $\gamma$ -rays and Data Reduction by a Least-Squares Method. J. Nucl. Sci. Technol. **48**, 834–840 (2011). doi:10.3327/jnst.48.834
- [28] I.Gheorghe, H.Utsunomiya, S.Katayama, et al., Photoneutron cross-section measurements in the <sup>209</sup>Bi ( $\gamma$ ,  $xn$ ) reaction with a new method of direct neutron-multiplicity sorting. Phys. Rev. C **96**, 044604 (2017). doi:10.1103/PhysRevC.96.044604
- [29] L.X.Liu,H.Utsunomiya,G.T.Fan, et al., Energy profile of laser Compton slant-scattering  $\gamma$ -ray beams determined by direct unfolding of total-energy responses of a BGO detector. Nucl. Instrum. Methods Phys. Res. Sect. A-Accel. Spectrom. Dect. Assoc. Equip. **1063**, 169314 (2024). doi:10.1016/j.nima.2024.169314
- [30] Z.C.Li,Y.Yang,Z.W.Cao, et al., Effective extraction of photoneutron cross-section distribution using gamma activation and reaction yield ratio method. Nucl. Sci. Tech. **34** (2023). doi:10.1007/s41365-023-01330-z
- [31] Z.R.Hao,L.X.Liu,Y.Zhang, et al., <sup>197</sup>Au( $\gamma$ ,n) cross section RAW data[DS/OL]. V1. Science Data Bank, 2025[2025-01-07]. doi:10.57760/sciencedb.19543
- [32] Z.R.Hao,L.X.Liu,Y.Zhang, et al., <sup>159</sup>Tb( $\gamma$ ,n) photoneutron cross section RAW data[DS/OL]. V1. Science Data Bank, 2025[2025-01-07]. doi:10.57760/sciencedb.19552
- [33] R.Z.Hao,L.X.Liu,Y.Zhang, et al., <sup>197</sup>Au( $\gamma$ ,n) and <sup>159</sup>Tb( $\gamma$ ,n) cross section[DS/OL]. V1. Science Data Bank, 2025[2025-01-07]. doi:10.57760/sciencedb.19582
- [34] MiniPIX TPX from ADVACAM, a miniaturized and low-power radiation camera, <https://advacam.com/camera/minipix-tpx3/>